Applied Catalysis B: Environmental 111–112 (2012) 467–475

Contents lists available at SciVerse ScienceDirect

Applied Catalysis B: Environmental

journal homepage: www.elsevier.com/locate/apcatb

Investigation of catalytic mechanism of formaldehyde oxidation over three-dimensionally ordered macroporous Au/CeO_2 catalyst

Baocang Liu[a,b], Changyan Li[a,b], Yifei Zhang[b], Yang Liu[a], Wenting Hu[a], Qin Wang[a], Li Han[c], Jun Zhang[a,b,*]

[a] College of Chemistry and Chemical Engineering, Inner Mongolia University, Hohhot 010021, PR China
[b] College of Life Science, Inner Mongolia University, Hohhot 010021, PR China
[c] Baotou Research Institute of Rare Earths, Baotou 014030, PR China

ARTICLE INFO

Article history:
Received 10 July 2011
Received in revised form 19 October 2011
Accepted 24 October 2011
Available online 6 November 2011

Keywords:
Three-dimensionally ordered macroporous material
Au/CeO_2 catalyst
Formaldehyde oxidation
Catalytic mechanism

ABSTRACT

A colloidal crystal template method coupled with a precursor complexion process was developed to create three-dimensionally ordered macroporous (3DOM) Au/CeO_2 catalyst. The resultant Au/CeO_2 catalyst possesses well-defined 3DOM structure, and shows enhanced catalytic performance for formaldehyde (HCHO) oxidation with 100% HCHO conversion at ~75 °C. The catalytic mechanism of HCHO catalytic oxidation over 3DOM Au/CeO_2 catalyst was systematically investigated by means of gas chromatograph (GC), H_2-temperature programmed reduction (H_2-TPR), temperature programmed surface reaction (TPSR), CO_2-temperature programmed desorption (TPD), and Fourier transform infra-red (FT-IR) spectroscopy. GC results indicate that HCOOH intermediate is generated during HCHO catalytic oxidation. TPD and TPSR tests show that the weak absorption ability of CO_2 over 3DOM Au/CeO_2 catalyst and the existence of Au active species in ionic and metallic states in 3DOM Au/CeO_2 catalyst largely improve the catalytic activity, favoring the enhanced HCHO catalytic oxidation. FT-IR tests prove that the carbonate and hydrocarbonate formed on the surface of 3DOM Au/CeO_2 catalyst during HCHO catalytic oxidation may account for its deactivation. Based on the above investigation, a new catalytic mechanism of enhanced HCHO catalytic oxidation over 3DOM Au/CeO_2 catalyst is proposed. The mechanism may afford the scientific guidance for preparing high efficiency oxide supported noble metal catalysts and present a solution for solving their deactivation problem.

1. Introduction

With the broad applications of decorating and furnishing materials, the formaldehyde (HCHO) is becoming one of the most concerned indoor air pollutants. It may cause serious health problems including burning sensations in eyes and throat, nausea, difficulty in breathing, and even lethiferous diseases such as nasopharyngeal or nasal cancer, when living in a room with the prolonged exposure to concentrations of HCHO that exceed safe limitations [1,2]. Thus, indoor air pollution has already aroused increasing concern, and great efforts have been made to eliminate HCHO pollution [3–14]. Low temperature catalytic oxidation of HCHO is regarded as one of most attractive approaches for the elimination of HCHO, as HCHO can be completely converted into CO_2 and H_2O through catalytic oxidation process. In this case, efficient catalysts that can realize the low temperature catalytic oxidation of HCHO into CO_2 and H_2O are highly needed.

Recently, great progress has been made on the supported noble metallic catalysts, such as Au/CeO_2 [3,5,6], Au/Co_3O_4–CeO_2 [7], $Ag/MnOx$–CeO_2 [8], $Pt/MnOx$–CeO_2 [9], Pd/TiO_2 [10], Pt/TiO_2 [11,12], Pt/Fe_2O_3 [13,5], Au/ZrO_2 [14,15], $PdMn/Al_2O_3$ [16] etc., for HCHO catalytic oxidation due to their high catalytic efficiency. The HCHO can be completely converted into CO_2 and H_2O over the supported noble metallic catalysts via catalytic oxidation process, for instance, the complete conversion of HCHO into CO_2 and H_2O can be realized via catalytic oxidation process over Au/CeO_2 at ~75 °C [3], and over $Pt/MnOx$–CeO_2 [9] and Pt/TiO_2 [10] catalysts around room temperature. Thus, the supported noble metal catalysts are believed to be one kind of effective catalysts for HCHO catalytic oxidation at relatively low temperature.

Among the most effective supported noble metal catalysts, oxide-supported Au catalysts, especially Au/CeO_2, exhibits extraordinarily high activity in many reactions including HCHO catalytic oxidation at moderate temperatures [3,5–7,14,15], and therefore are expected to be valuable catalyst systems for effective catalytic removal of HCHO. However, the aggregation of Au nanoparticles

* Corresponding author at: College of Chemistry and Chemical Engineering, Inner Mongolia University, Hohhot 010021, PR China. Tel.: +86 471 4992175; fax: +86 471 4992278.
E-mail address: cejzhang@imu.edu.cn (J. Zhang).

0926-3373/$ – see front matter © 2011 Elsevier B.V. All rights reserved.
doi:10.1016/j.apcatb.2011.10.036

on powder catalyst supports during the preparation largely affects their catalytic activity, since the aggregation may lead to the formation of larger particles and reduce the catalyst surface areas, eventually lowering their catalytic activity. We have recently reported the preparation of three-dimensionally ordered macroporous (3DOM) Au/CeO_2 catalysts with superior catalytic property for HCHO catalytic oxidation [3]. Comparing with the powder Au/CeO_2 catalysts, their catalytic property is greatly enhanced due to less aggregation and good distribution of key catalyst species on 3DOM CeO_2 supports. However, the catalytic mechanism of 3DOM Au/CeO_2 catalysts for enhanced HCHO catalytic oxidation has not been fully presented. Therefore, this work aims at further systematically clarifying the catalytic mechanism of enhanced HCHO catalytic oxidation over 3DOM Au/CeO_2 catalysts.

In this paper, 3DOM Au/CeO_2 catalysts were created via colloidal crystal template method coupled with a precursor complexion process. Scanning electron microscope (SEM) and transmission electron microscope (TEM) were employed to characterize the microstructure, size and morphology of the obtained 3DOM Au/CeO_2 catalysts, and the catalytic mechanism of the catalysts was systematically studied by means of gas chromatograph (GC), temperature programmed desorption (TPD), temperature programmed reduction (TPR), temperature programmed surface reaction (TPSR), and Fourier transform infra-red (FT-IR) spectroscopy. The results show that HCOOH intermediate is generated during HCHO catalytic oxidation. The weak absorption ability of CO_2 over 3DOM Au/CeO_2 catalyst and the existence of Au active species in 3DOM Au/CeO_2 catalyst account for the improvement of catalytic activity. The carbonate and hydrocarbonate formed on the surface of 3DOM Au/CeO_2 catalyst during HCHO catalytic oxidation are responsible for the deactivation of 3DOM Au/CeO_2 catalyst. The mechanism may afford the scientific guidance for preparing high efficiency oxide supported noble metal catalysts and present a solution for solving their deactivation problem.

2. Experimentals and methods

2.1. Catalyst preparation

2.1.1. Synthesis of monodispersed PS colloidal spheres

The preparation of monodispersed PS colloidal spheres follows the similar procedures as the one was previously reported [3,17,18]. Typically, a certain amount of pre-treated St monomer (6 mL) and distilled water (170 mL) were added to a 250 mL three neck round-bottomed flask under nitrogen protection. The mixture was magnetically stirred, and 10 mL $K_2S_2O_8$ (KPS) solution (0.007 g/mL) was added into the mixture to initiate the polymerization reaction at 70 °C for 28 h. After the reaction was finished, the homogenous latex with nearly monodispersed PS particles with average diameters around 200 nm was collected.

2.1.2. Assembly of three-dimensionally ordered PS colloidal crystal templates

Three-dimensionally ordered PS colloidal crystal templates were assembled via a centrifugation method [3,19]. A certain amount of PS latex consisting of monodispersed PS colloidal spheres was ultrasonicated to form a uniform emulsion and centrifuged. After the PS colloidal spheres were fully precipitated, the supernatant was carefully removed. The centrifuge tube containing the well-arranged PS colloidal spheres was then naturally dried to obtain the highly ordered three-dimensional PS colloidal crystal templates for use in synthesizing 3DOM CeO_2.

2.1.3. Synthesis of 3DOM CeO_2 via a precursor complexion process

The synthesis of 3DOM was carried out following a reported method with slight modification [3,20]. Equal molar citric acid (1.05 g) and $Ce(NO_3)_3{\cdot}6H_2O$ (2.17 g) were dissolved in 95% ethanol (10 mL) to form a precursor solution. The citric acid was employed here to be a chelating ligand to form stable complex with rare earth ions, providing a higher melting point and a good compatibleness with PS template [21]. The three-dimensionally ordered PS colloidal templates were carefully placed into a Buchner funnel, to which a vacuum was applied. Then, the precursor solution was dropped into the funnel until the PS colloidal crystal templates were completely permeated, following the filtration and drying at 65 °C for 90 min. The above procedures were repeated for four times to ensure the complete permeation of citric acid and $Ce(NO_3)_3$ precursor solution into the interstices of PS colloidal crystal templates. The obtained PS colloidal templates filled with citric acid and $Ce(NO_3)_3$ precursor solution were annealed at 500 °C at a heating rate of 3 °C min^{-1} for 5 h to remove the PS colloidal templates to form 3DOM CeO_2. Due to the shrinkage of PS sphere templates during calcination process, the pore sizes of 3DOM CeO_2 supports prepared by using 200 nm PS spheres as templates were approximately 80 nm, respectively.

2.1.4. Synthesis of 3DOM Au/CeO_2 catalysts

The synthesis of 3DOM Au/CeO_2 catalysts was carried out via a gas bubbling-assisted deposition precipitation method developed in our lab [3]. The typical preparative procedures were described as follows: 3DOM CeO_2 (0.2 g) supports with pore sizes of 80 nm were introduced into the diluted $HAuCl_4$ solution (12.6 mL, 1 g/L) to form a suspension. A gas bubbling-assisted stirring operation was employed to agitate the suspension for 0.5 h. Then, the pH value of the suspension was adjusted to 9 by adding Na_2CO_3 (0.2 mol/L) to precipitate Au ions. The reaction system was further vigorously bubbled with air for 2 h, and let stand for 24 h. The product was filtered and washed until Cl^- was completely removed, and the final products were dried in an oven at 60 °C to obtain the desired 3DOM Au/CeO_2 catalysts. According to atomic emission spectroscope (AES) measurement, the actual Au loading content of 3DOM Au/CeO_2 is estimated to be around 0.56 wt.% under the present preparation condition with the theoretical Au loading content at 3 wt.%.

2.2. Characterization

Powder X-ray diffraction (XRD) was used to characterize the phase structures of 3DOM Au/CeO_2 catalysts. Measurements were performed using a Bruker AXS-D8 diffractometer (German) operated at 40 kV and 40 mA with a slit of 1/2 at a scanning rate of 3° min^{-1} in a scanning range of $2\theta = 20–80°$, using Cu Kα radiation ($\lambda = 0.15406$ nm). Samples for XRD measurement were prepared by gently crushing the obtained products with a mortar and pestle, and were placed in a quartz glass holder for characterization. Transmission electron microscopy (TEM) was performed on a JEM-2010 system operated at an acceleration voltage of 120 kV to evaluate the structure, geometry, pore size, and Au distribution in 3DOM Au/CeO_2 catalyst. Samples for TEM analysis were prepared by drying a drop of PS latex or catalyst dispersion on an amorphous carbon-coated copper grid for observation. Scanning electron micrographs were recorded with a Hitachi S-3400N scanning electron microscopy (SEM) to determine the PS sizes, colloidal crystal arrangement, and catalyst pore size. Samples for SEM measurement were deposited on silicon substrates and coated with a 5 nm Pt for characterization. Energy dispersive spectroscopy (EDS) was performed with an EDAX attached to an SEM. The Fourier transform infrared (FT-IR) spectra were scanned in range

of 4000–400 cm^{-1} using a MAGNA-IR750 type FT-IR spectrometry at a resolution of 0.1 cm^{-1} to characterize the intermediates and reaction products of HCHO catalytic oxidation on catalyst surface. The samples were prepared by mixing certain amount of catalyst with KBr and gently crushing with a mortar and pestle, and then were pressed into pallets under the pressure of 15 Mpa for characterization. X-ray photoelectron spectroscopy (XPS) measurements were carried out on a XSAM800 X-ray photoelectron spectrometer with an Al Kα (1486.67 eV) excitation source to determine the existence and valence states of Au nanoparticles in the catalysts. Samples annealed at different temperatures were used for characterization. Actual Au content in the catalysts was estimated with a VARIAN VISTA-MPX atomic emission spectroscope (AES, USA).

2.3. Catalytic activity testing

The catalytic activity tests were carried out in a continuous-flow fixed-bed reactor consisting of a glass tube (inner diameter 0.8 cm) attached on a PX-200 catalyst characterization system (Tianjin Pengxiang Co., Ltd.). A gas chromatograph (GC-2014C, Shimadzu) was equipped on PX-200 catalyst characterization system for on-line analysis of the products. The reaction products were separated with two chromatograph columns. A GDX-403 chromatographic column was used to separate the unreacted HCHO and intermediate HCOOH. A molecular sieve chromatographic column was employed to separate the generated CO_2. A TCD detector was applied to on-line monitor the products. 200 mg catalyst was loaded into the reactor. The feeding gas was 0.06 vol.% HCHO balanced with the air generated by passing an air flow, which was previously passed through 5 A zeolites and solid NaOH to remove H_2O and CO_2, through a solution of 36 wt.% HCHO at 0 °C. The space velocity of the experiment was 6.6×10^4 mL h^{-1} g^{-1}. The activity of the catalysts on HCHO oxidization was estimated by the conversion rate of CO_2 following a HCHO oxidation process. The concentration of CO_2 resulting from HCHO oxidation was measured with gas chromatograph (GC-2014C, Shimadzu) equipped on PX-200 catalyst characterization system to online estimate the HCHO oxidation. The detailed experiments were conducted following the procedures described as follows: First, the gas, which had been pre-cleaned to remove H_2O and CO_2, was continuously flowed through Au/CeO_2 catalysts in the reactor. The reactor was then heated to 80 °C to remove the substances adsorbed on the surface of the catalysts and subsequently cooled to room temperature. Next, the feeding gas containing 0.06 vol.% HCHO was introduced into the reactor continuously. The reactor was heated to different temperatures under air flow (220 mL min^{-1}) to evaluate the temperature-dependant catalytic activity of the catalysts. The absorbed HCHO will be catalytically converted into CO_2 following a HCHO oxidation reaction. The resulting CO_2 released from the reactor due to the HCHO oxidation can be analyzed online with gas chromatograph.

2.4. H_2-TPR

H_2-TPR measurements were carried out with a PX-200 catalytic characterization system equipped with gas chromatograph. A TCD detector in gas chromatograph was used. About 50 mg catalyst was loaded and pretreated with N_2 at 80 °C for 30 min to remove the adsorbed carbonates and hydrates. After cooling down to room temperature and introducing the reduction agent of 5% H_2/N_2 with a flow rate of 50 mL min^{-1}, the temperature was then programmed to rise at a ramp of 10 °C min^{-1} to obtain H_2-TPR data. H_2 consumption was monitored by TCD and calibrated by carrying out the reduction of CuO.

2.5. CO_2-TPD

CO_2-TPD tests were conducted using PX-200 catalytic characterization system equipped with a gas chromatograph. A TCD detector in gas chromatograph was used. Prior to each TPD run, about 0.1 g catalyst was pretreated in He flow at 300 °C in a quartz reactor. After the reactor temperature was lowered to room temperature, the catalyst was treated with CO_2 for 60 min with a gas flow (CO_2:He = 1:4) of 50 mL min^{-1} to enable the absorption of CO_2. Then, He gas was introduced into the reactor at a rate of 50 mL min^{-1} for 30 min to remove residual oxygen. The catalyst was then heated to 750 °C at a constant heating rate of 10 °C min^{-1} under He flow of 50 mL min^{-1}. The desorbed CO_2 was monitored by TCD detector.

2.6. TPSR

TPSR experiments were performed to acquire the information of adsorbed species, HCHO and O_2 on catalyst surface during the reaction. About 50 mg catalyst was loaded into the reactor, and purged with high purity He (99.995%). The temperature of the reactor was increased linearly from ambient to 150 °C in order to remove the substances absorbed on the catalyst surface. The Au/CeO_2 catalyst was then cooled down to ambient temperature in the flow of high purity He, following with the introduction of HCHO and O_2 carried by purified air. The HCHO flowed through the reactor for 30 min, allowing the substances involved to adsorb on the catalyst. Then, high purity He was introduced into the reactor to remove the unabsorbed substances, and the reactor temperature was increased at a designed rate of 10 °C min^{-1} in a flow of high purity He to allow the oxidation reaction to take place. The oxidation products in the effluent gas from the reactor were analyzed by TCD detector.

3. Results and discussion

3.1. Colloidal crystal templates, 3DOM CeO_2 supports, and 3DOM Au/CeO_2 catalysts

Our previous work has reported the fabrication of PS microspheres, the assembly of colloidal crystal templates, and the synthesis of 3DOM CeO_2 supports and Au/CeO_2 catalysts in details [3], and this work aims at the investigation of catalytic mechanism of HCHO over such catalysts. Fig. 1 presented the typical SEM images (a and b) and TEM images (c and d) of 200 nm PS colloidal microspheres, 3DOM CeO_2 support, and 3DOM Au ~0.56 wt.%/CeO_2 catalyst prepared by using 200 nm PS colloidal microspheres as templates, respectively. It is revealed from Fig. 1(a) that the obtained PS colloidal microspheres are highly uniform with narrow size distribution, and can be closely packed into a highly ordered three-dimensional arrangement. The average sizes of PS microspheres in colloidal crystal arrays are estimated to be around 200 nm. By using the colloidal crystal arrays as templates, 3DOM CeO_2 support is created via a precursor complexion process, as the SEM image is shown in Fig. 1(b), which reveals that the formed CeO_2 has well-defined 3DOM structures. The pore sizes of 3DOM CeO_2 can be deduced from Fig. 1(b and c) to be approximately 80 nm, much smaller than the original PS colloidal microsphere templates due to the calcination shrinkage [22]. The interconnected networks of the ordered macropore structures of 3DOM CeO_2 can be clearly observed. Thus, by using PS colloidal crystal arrays as templates, 3DOM CeO_2 can be successfully fabricated.

By using 3DOM CeO_2 as support, 3DOM Au/CeO_2 catalyst with 80 nm pore sizes and ~0.56 wt.% Au loading content can be successfully synthesized via a gas bubbling-assisted deposition precipitation approach. The 3DOM Au/CeO_2 catalyst obtained by our method has relatively low Au loading content compared with that synthesized by co-precipitation method. This may be due to the

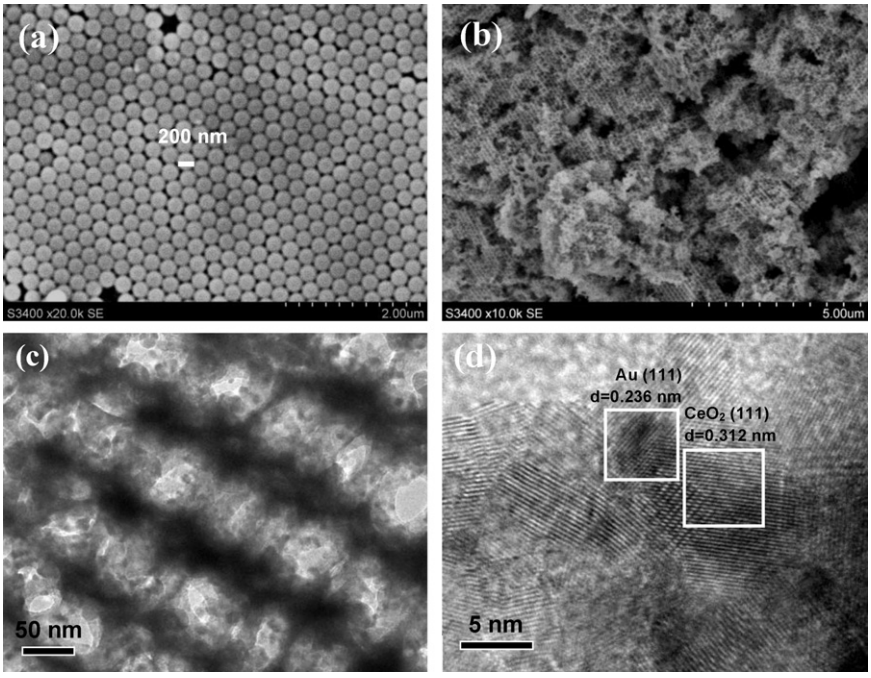

Fig. 1. Typical SEM images (a and b) and TEM images (c and d) of 200 nm PS colloidal microspheres (a), 3DOM CeO_2 support (b), and (c and d) 3DOM Au ~0.56 wt.%/CeO_2 catalyst prepared by using 200 nm PS colloidal microspheres as templates.

fact that the gas bubbling agitating method used in our preparation may cause the insufficient agitation, and the 3DOM Au/CeO_2 catalyst presents relatively small specific surface, which may also account for the low Au loading content. Fig. 1(c) displays the typical TEM images of 3DOM Au/CeO_2 catalyst with Au loading content at ~0.56 wt.% on 3DOM CeO_2 support with 80 nm pore sizes synthesized by using 200 nm PS colloidal microspheres as templates. As it is shown in Fig. 1(c), after the in situ formation of Au nanoparticles on 3DOM CeO_2 support, the Au/CeO_2 catalyst still maintains well-defined 3DOM structure, without the occurrence of obvious Au nanoparticles blocking behavior, suggesting the well distribution of Au nanoparticles on 3DOM CeO_2 support. The interconnected networks of 3DOM Au/CeO_2 pore structure are obviously observed, further confirming the well-defined three-dimensionally ordered hexagonal structure of Au/CeO_2 catalyst with Au nanoparticles distributed on CeO_2 support. The HRTEM image in Fig. 1(d) further clearly indicates the lattice fringes of 0.236 and 0.312 nm indexed to Au (1 1 1) and CeO_2 (1 1 1) of 3DOM Au/CeO_2. The sizes of Au nanoparticles formed on the surface of 3DOM CeO_2 support are estimated to be around 5 nm. To confirm the formation and phase structure of 3DOM Au/CeO_2, EDS and XRD characterizations were conducted (data not shown). It is proven by EDS measurement that the representative peaks corresponding to Ce, Au, and O elements are existed in the 3DOM Au/CeO_2 catalyst, implying the formation of Au/CeO_2 catalyst. The result is consistent with the XRD characterization, as XRD pattern clearly illustrates the formation of cubic phased CeO_2. The broad diffraction feature of Au/CeO_2 catalysts implies the formation of macroporous structures.

3.2. Catalytic performance on HCHO oxidation

3.2.1. Catalytic activity of 3DOM Au/CeO_2 catalyst

The performance of 3DOM Au/CeO_2 catalysts with different pore sizes and Au loading contents for HCHO catalytic oxidation in our previous investigation displays that when loading with the same Au content, the 3DOM Au/CeO_2 catalyst with 80 nm pore size shows superior catalytic activity for HCHO catalytic oxidation due to its higher surface area. When fixing the pore size of 3DOM Au/CeO_2 catalyst at 80 nm, the catalytic performance for HCHO oxidation is largely affected by the Au loading content. It is indicated that the 3DOM Au/CeO_2 catalyst with Au loading content at ~0.56 wt.% possesses the most efficient catalytic activity with 30% conversion of HCHO at room temperature and 100% conversion at ~75 °C, approximately 25 °C lower than previously reported Au/CeO_2 catalyst [3,5,6]. The 3DOM structure of Au/CeO_2 catalyst with interconnected networks of spherical voids favoring the less aggregation and good distribution of small Au nanoparticles may account for their enhanced catalytic activity. Thus, 3DOM Au ~0.56 wt.%/CeO_2 catalyst with 80 nm pore size is an ideal candidate for studying the catalytic mechanism for enhanced HCHO catalytic oxidation.

Fig. 2(a) presents the GC diagrams showing the reaction intermediates and products of HCHO catalytic oxidation over 3DOM Au ~0.56 wt.%/CeO_2 catalyst. It can be found that the chromatograph peaks indexed to air, CO_2, HCHO, H_2O, CH_3OH, and HCOOH are obviously detected. The air, HCHO and CH_3OH peaks appeared in GC diagrams are arisen from the original feeding gaseous stream [23,24]. The CO_2 and H_2O are the reaction products of the catalytic oxidation of HCHO. The HCOOH is estimated to be the reaction intermediate of HCHO catalytic oxidation over 3DOM Au/CeO_2 catalyst, which was also evidenced in previous reports [7,25–28] and further proven by our FT-IR characterization, which will be discussed later. Fig. 2(b) shows the enlargement diagram of CO_2 generated during the catalytic oxidation of HCHO, from which it can be seen that the CO_2 content is gradually increased with the increase of catalytic oxidation temperature of HCHO, reaching to the highest around 75 °C, indicating the complete oxidation of HCHO. Conversely, the amount of HCHO is decreased with the increase of catalytic oxidation temperature of HCHO as shown in Fig. 2(c), completely disappeared around 75 °C, suggesting the complete conversion of HCHO into CO_2 and H_2O. Interestingly, it is worth noted that the content of HCOOH intermediate is gradually generated with the increase of catalytic oxidation temperature of HCHO in low temperature range as shown in Fig. 2(d), reaching to the highest when increasing the temperature to 25 °C. Further increasing the temperature causes the decrease of HCOOH content, which totally disappears around 75 °C. This implies that HCHO is

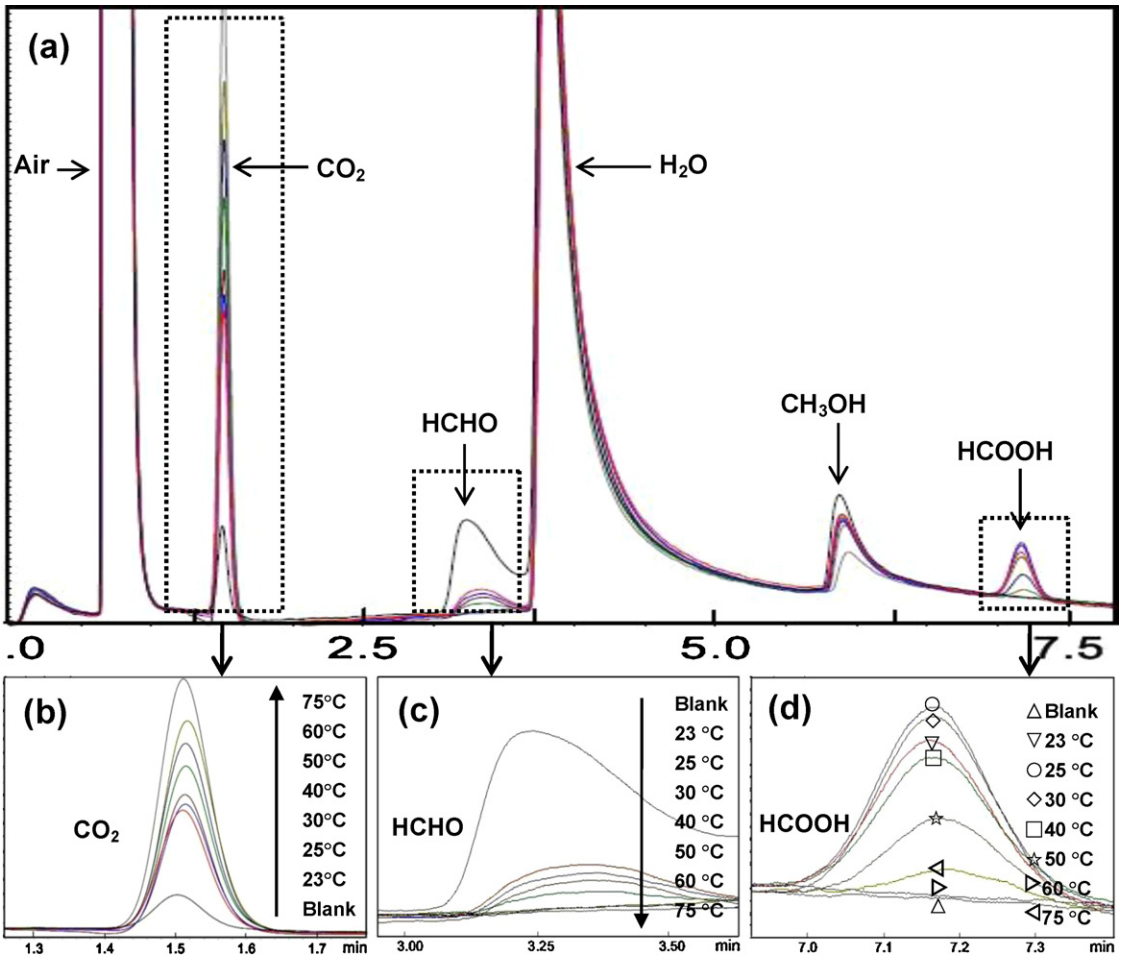

Fig. 2. The GC diagrams online monitoring the HCHO catalytic oxidation over 3DOM Au ~0.56 wt.%/CeO_2 catalyst. (a) GC diagram for the detection of air, CO_2, HCHO, H_2O, CH_3OH, and HCOOH, and enlargement of chromatograph peaks of (b) CO_2, (c) HCHO, and (d) HCOOH.

not directly oxidized into CO_2 and H_2O in the initial stage, and the HCOOH intermediate exists during HCHO catalytic oxidation process, which means that the HCHO is firstly oxidized into HCOOH, and then the HCOOH is subsequently converted into CO_2 and H_2O [25–28].

3.2.2. H_2-TPR test

Fig. 3 indicates the H_2-TPR test of 3DOM CeO_2 support and 3DOM Au ~0.56 wt.%/CeO_2 catalyst. There are only two reduction peaks in H_2-TPR measurement for 3DOM CeO_2. The peak located at

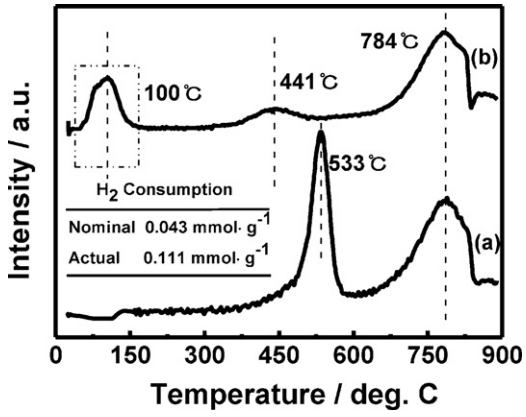

Fig. 3. The H_2-TPR measurement of (a) 3DOM CeO_2 support and (b) 3DOM Au ~0.56 wt.%/CeO_2 catalyst.

533 °C is resulted from the reduction of surface Ce^{4+} absorbed O_2^- and O^{2-} species, [29–33] while the peak appeared at 784 °C is due to the partial reduction of lattice CeO_2 into Ce_2O_3. [29,30] However, after loading Au into 3DOM CeO_2, three peaks located at 100, 441, and 784 °C are observed for 3DOM Au ~0.56 wt.%/CeO_2. The peak located at 441 °C is still ascribed to the reduction of surface Ce^{4+}, absorbed O_2^- and O^{2-} species, which shifts to 441 °C from 553 °C due to the incooperation of Au activating the CeO_2. Moreover, one peak located at 100 °C is newly observed, which attributes to the reduction of ionic Au. This reduction peak makes the major contribution to HCHO oxidation in comparison with the other two reduction peaks in high temperature region around 441, and 784 °C. To further study the interaction between Au and CeO_2, the calibrated H_2 consumption of the reduction peak in low temperature at 100 °C was measured, as the results were shown in Fig. 3. The actual H_2 consumption estimated to be 0.111 mmol g^{-1} is higher than the nominal H_2 consumption of 0.043 mmol g^{-1} calculated by assuming all present as Au^{3+} in the catalyst, suggesting a co-reduction of CeO_2 due to a typical H_2 spillover effect [34]. This means that CeO_2 could be reduced to form a redox couple with ionic Au during HCHO oxidation process, proving that CeO_2 also plays an important role in catalytic process of HCHO oxidation, largely supporting the proposed catalytic mechanism, which will be discussed later. The large deviation between the actual and nominal H_2 consumption implies the enhanced reduction capability of 3DOM Au ~0.56 wt.%/CeO_2 due to the strong interaction between ionic Au and CeO_2.

The lowering of reduction temperature implies that the presence of Au helps to weaken the surface oxygen on CeO_2, and

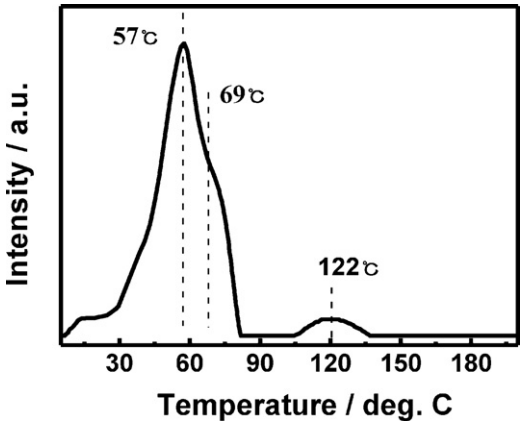

Fig. 4. The HCHO-TPSR characterization of 3DOM Au ~0.56 wt.%/CeO_2 catalyst.

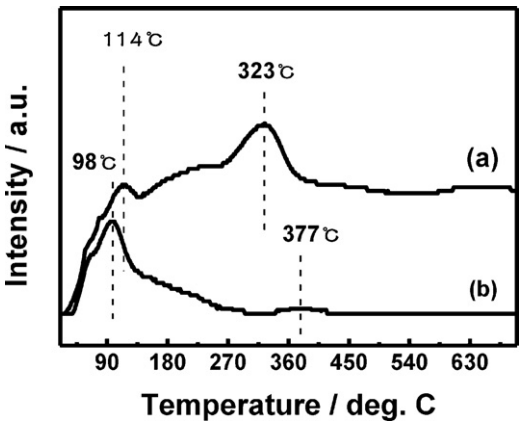

Fig. 5. The CO_2-TPD characterization of (a) 3DOM CeO_2, support (b) 3DOM Au ~0.56 wt.%/CeO_2 catalyst.

therefore, improves the reducibility of the catalyst [13,14,33,35]. This facilitates the oxygen to transfer across the solid–gas interface during the reaction. The reduction peak featuring the low temperature and narrow width suggests the existence of small Au nanoparticle with narrow size distribution [36–39].

3.2.3. HCHO-TPSR measurement

Fig. 4 displays the HCHO-TPSR measurement of 3DOM Au ~0.56 wt.%/CeO_2 catalyst. Three reaction peaks located at 57, 69 and 122 °C are clearly observed. The two reaction peaks in low temperature are indexed to the reaction of HCHO into CO_2, while the reaction peak in high temperature is ascribed to the desorption of CO_2 previously absorbed on the surface of the catalyst [14]. It is interesting that the splitting of the peaks in low temperature is clearly observed. This suggests that there are two forms of Au in ionic and metallic states existing in the catalyst with different catalytic activities. It is revealed that ionic state Au shows higher catalytic activity than metallic state Au [3,40]. Thus, the peaks at 57 and 69 °C are ascribed to the oxidation of HCHO into CO_2 with ionic state Au, and metallic state Au, respectively, while the peak at 122 °C is due to the desorption of the adsorbed CO_2 generated during HCHO oxidation process. From Fig. 4, it is also deduced that the content of ionic state Au is much more than metallic state Au, accounting for the higher catalytic activity, which has also been proven by XPS results. The HCHO-TPSR test shows that the oxidation of HCHO into CO_2 and H_2O occurs within 20–75 °C, which is consistent with the previous catalytic performance results.

3.2.4. CO_2-TPD characterization

The CO_2-TPD tests of 3DOM CeO_2 support and 3DOM Au ~0.56 wt.%/CeO_2 catalyst are given in Fig. 5. It is found that the CO_2 desorption temperature has large effect on catalytic activity of the catalyst. The active site having lower CO_2 desorption temperature possesses the higher catalytic activity [7]. A strong and weak desorption peaks located at 114 and 323 °C were clearly observed in 3DOM CeO_2. While two desorption peaks around 98 and 377 °C could be detected as well in 3DOM Au ~0.56 wt.%/CeO_2. Comparing with 3DOM CeO_2, two desorption peaks of 3DOM Au ~0.56 wt.%/CeO_2 catalyst shift to lower and higher temperature, respectively, and the intensity of the desorption peak in low temperature is increased largely, while that of the desorption peak in high temperature is decreased obviously. This suggests that the surface characteristics of 3DOM CeO_2 support changes after the loading of Au nanoparticles. More weak basic sites are generated, and the middle strong basic sites are reduced, causing the easier desorption of CO_2 from 3DOM Au ~0.56 wt.%/CeO_2 catalyst, and thus improving the catalytic activity [41,42].

This phenomena suggests that the desorption of CO_2 from 3DOM Au ~0.56 wt.%/CeO_2 catalyst may be a key step for HCHO catalytic oxidation reaction. The desorption peak located in high temperature might be ascribed to the interaction of CO_2 with the support surface to form carbonate and hydrocarbonate, which may cause the deactivation of 3DOM Au ~0.56 wt.%/CeO_2 [6,43].

Due to the fact that the intensity of the desorption peak in low temperature is increased largely, and the intensity of the desorption peak in high temperature is decreased obviously, causing the easier desorption of CO_2 from the surface of Au ~0.56 wt.%/CeO_2, and the much difficult formation of carbonate and hydrocarbonate on the surface of Au ~0.56 wt.%/CeO_2. Thus, the catalytic activity is largely enhanced and the tendency of deactivation of the catalyst is lowered.

3.2.5. FT-IR measurement

To further confirm the formation of carbonate and hydrocarbonate during HCHO catalytic oxidation, FT-IR characterization was carried out. Fig. 6 presents the FT-IR spectra of 3DOM Au ~0.56 wt.%/CeO_2 catalyst after catalytic oxidation reaction. It can be seen from the FT-IR spectra that four IR peaks are detected, and each peak is splitted into two small peaks. The peaks located at 3459 and 3416 cm^{-1} can be indexed to the stretching vibration of O–H (ν_{O-H}) of H_2O absorbed on the surface of the catalyst. The intensity of the peak is increased initially, and decreased consequently with the increase of reaction temperature, indicating the initial increase and consequent decrease of absorbed H_2O content in the catalyst. The FT-IR peaks around 2361.5 and 2234.3 cm^{-1}

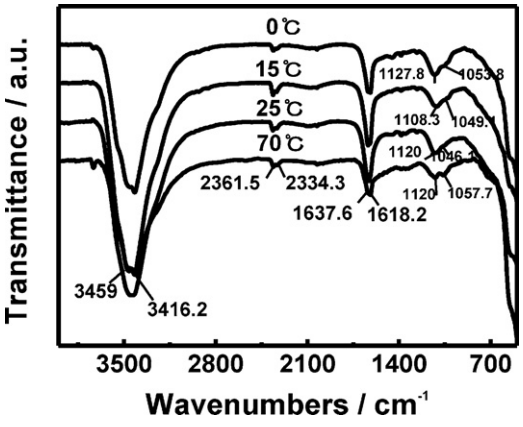

Fig. 6. FT-IR spectra of 3DOM Au ~0.56 wt.%/CeO_2 catalyst under different reaction temperature.

are resulted from the asymmetric stretching vibration of O=C=O ($\nu_{as\ O=C=O}$) of the absorbed CO_2, showing the similar change with the increase of reaction temperature. The FT-IR peak observed at 1637 cm^{-1} is ascribed to the face bending vibration of O–H (δ_{O-H}) of the absorbed H_2O on the surface of the catalyst. It is worth noted that three peaks located at 1618, 1050 and 1120 cm^{-1} are corresponding to the stretching vibration of C–O (νCO_3^{2-}) of carbonate and hydrocarbonate absorbed on surface of CeO_2 [43].

It has been reported that the catalytic oxidation of HCHO over Au/CeO_2 catalyst may cause the formation of carbonate and hydrocarbonate on the catalyst surface [6]. These carbonate and hydrocarbonate may occupy the active sites of the catalyst. Thus, in a consequence, the formation of carbonate and hydrocarbonate would largely affect the catalytic activity, and may cause the deactivation of the catalyst. 3DOM Au/CeO_2 catalyst possesses the large and open macroporous structure, and the blocking of the porosity by the formed carbonate and hydrocarbonate may be lessened, thus shows the enhanced catalytic activity for HCHO catalytic oxidation.

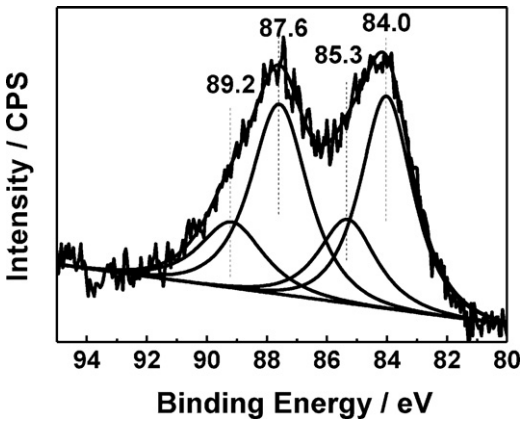

Fig. 7. Au4f XPS spectra of 3DOM Au ~0.56 wt.%/CeO_2 catalyst with 80 nm pore sizes.

3.3. Catalytic mechanism

Fig. 7 presents the Au4f XPS spectra of 3DOM Au ~0.56 wt.%/CeO_2 catalyst with 80 nm pore sizes. It is observed from Fig. 7 that the typical binding energies of Au4f7/2 (84.0 and 85.3 eV) and Au4f5/2 (85.3 and 89.2 eV) are assigned to Au^0 and Au^{3+}, respectively, suggesting that there are two valence states of ionic Au^{3+} and metallic Au^0 co-existing in 3DOM Au/CeO_2 catalyst.[5,6,44] In combination with H_2-TPR, and HCHO-TPSR measurements, it is deduced that the ionic Au^{3+} shows higher catalytic activity than metallic Au^0 for HCHO catalytic oxidation [3,5,6,14].

The GC characterization displays the generation of HCOOH intermediate, while FT-IR confirms the formation of carbonate

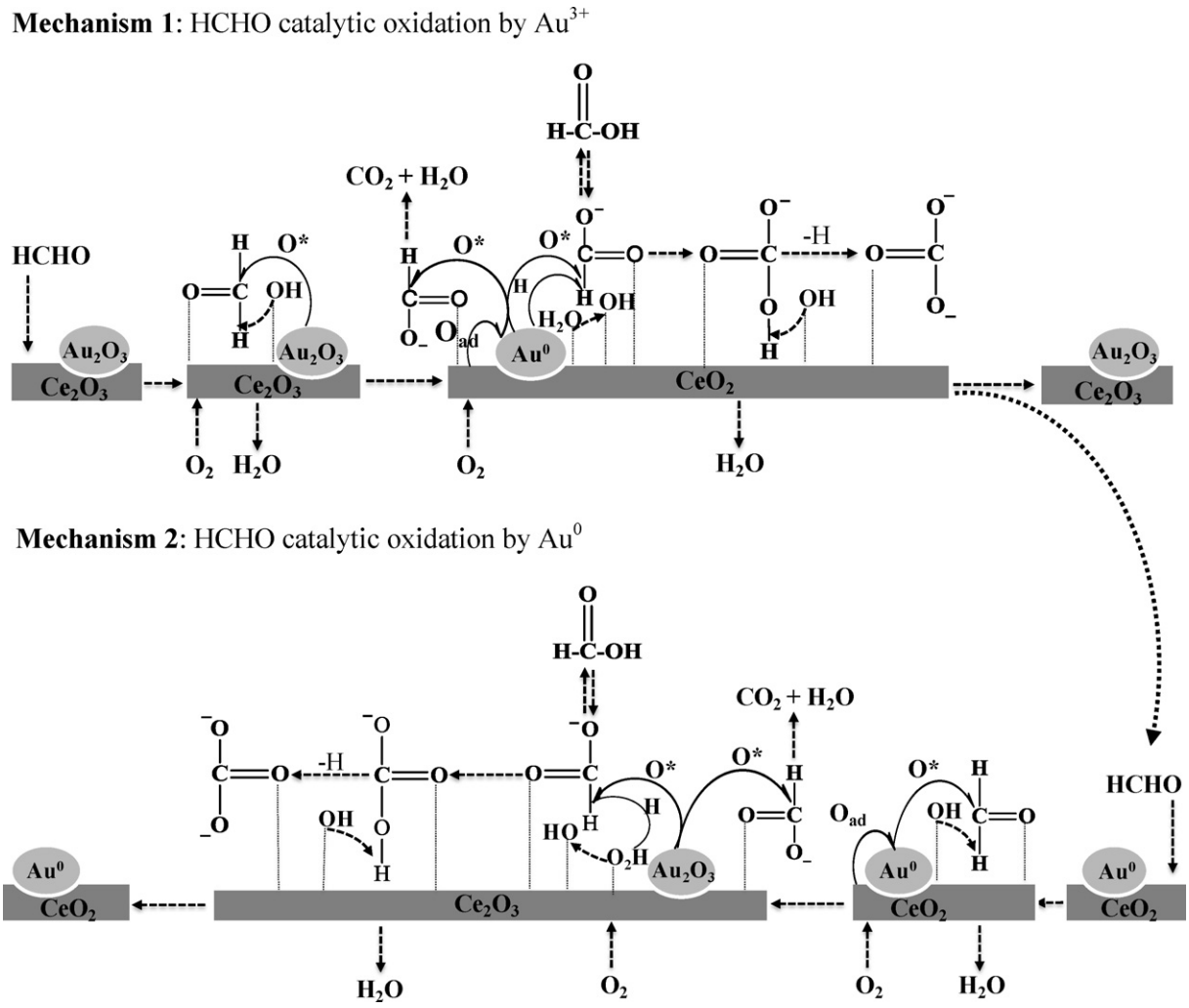

Scheme 1. The proposed catalytic mechanism of 3DOM Au ~0.56 wt.%/CeO_2 catalyst for enhanced HCHO catalytic oxidation.

and hydrocarbonate on the surface of 3DOM Au/CeO_2 catalyst during HCHO catalytic oxidation [3]. Similar results have been partially revealed before [25–28]. Based on the above investigations, the detailed catalytic mechanism of 3DOM Au/CeO_2 catalyst for enhancement of HCHO catalytic oxidation is proposed.

It is believed that the catalytic conversion of HCHO into CO_2 and H_2O over 3DOM Au/CeO_2 catalyst is experienced in two processes catalyzed by ionic Au^{3+} and metallic Au^0, respectively, in which ionic state Au^{3+} show higher catalytic activity. Scheme 1 illustrates the catalytic mechanism in detail. When Au^{3+} is formed on the surface of 3DOM Au/CeO_2 catalyst, the CeO_2 in contact with Au^{3+} may be partially reduced into Ce_2O_3. When HCHO is in contact with CeO_2 support, the absorption of HCHO onto the surface of CeO_2 support occurs. During this process, active oxygen may be transferred from Au_2O_3 to HCHO to form HCOOH and Au^0, and the HCOOH then changes into formate through the interaction with CeO_2 support, accompanying the losing of –H to form H_2O with free –OH absorbed on the surface of CeO_2 support. With the complete oxidation, HCOOH may be further converted into CO_2 and H_2O by continuously transferring the active oxygen to HCOOH. Meanwhile, the incomplete oxidation of HCOOH also occurs, this enables HCOOH to convert into carbonate and hydrocarbonate by losing one or two –H. When the lost –H interacts with the free –OH absorbed on the surface of CeO_2 support, H_2O is generated. Through this cycle, HCHO is converted into CO_2 and H_2O. The Au^{3+} in 3DOM Au/CeO_2 catalyst dominates the efficiency of the conversion of HCHO into CO_2 and H_2O.

When Au exists in metallic state, there may be another process for HCHO oxidation catalyzed by metallic state Au^0, but this process is believed not the dominant process for the efficient conversion of HCHO into CO_2 and H_2O. When the similar absorption of HCHO onto CeO_2 support is happened, the active oxygen is transferred to HCHO to form HCOOH, and then HCOOH is converted into CO_2 and H_2O following a complete oxidation process. However, the incomplete oxidation also happens simultaneously to form carbonate and hydrocarbonate, which may deactivate the catalytic activity of 3DOM Au/CeO_2 catalyst.

During HCHO catalytic oxidation process, there is an absorption and desorption balance for HCOOH to form formate on CeO_2 support, thus, the HCOOH can be converted into CO_2 and H_2O through the complete oxidation, and the formate can be changed into carbonate and hydrocarbonate as well following the incomplete oxidation, which deposits on the surface of CeO_2 support to deactivate the catalytic activity of the catalyst. Due to the large and open macroporous structure, the formed carbonate and hydrocarbonate may be hard to block the active sites of 3DOM Au/CeO_2 catalyst, which greatly enhances the catalytic activity 3DOM Au/CeO_2 catalyst for HCHO catalytic oxidation.

4. Conclusion

In this paper, a colloidal crystal template method coupled with a precursor complexion process was developed to synthesize novel 3DOM Au/CeO_2 catalyst. The synthesized Au/CeO_2 catalyst shows well defined 3DOM structure, and exhibit the enhanced catalytic activity for HCHO catalytic oxidation. The H_2-TPR, HCHO-TPSR, CO_2-TPD, and FT-IR characterizations reveal that the weak absorption ability of CO_2 over 3DOM Au/CeO_2 catalyst and the coexistence of Au active species of Au^{3+} and Au^0 may account for the efficient HCHO catalytic oxidation. The formation of carbonate and hydrocarbonate on the surface of 3DOM Au/CeO_2 catalyst derived from the incomplete oxidation of formate during HCHO catalytic oxidation process may lead to the deactivation of catalytic activity of 3DOM Au/CeO_2 catalyst. However, the formed carbonate and hydrocarbonate may be relatively hard to block the active sites on 3DOM Au/CeO_2 catalyst due to its large and open macroporous structure. Therefore, the 3DOM Au/CeO_2 catalyst shows the efficient catalytic activity for HCHO catalytic oxidation. The catalytic mechanism of HCHO oxidation over 3DOM Au/CeO_2 catalyst may afford the guidance for preparation of new catalysts available for effective elimination of HCHO through catalytic oxidation process.

Acknowledgements

We gratefully acknowledge the financial supports from National High Technology Research and Development Program (863 program, 2010AA03A407), National Natural Science Foundation of China (20961005), Project of Scientific Research of Inner Mongolia Autonomous Region for Institution of Higher Education (327011), Key Project of Natural Science Foundation of Inner Mongolia Autonomous Region, Department of Science and Technology of Inner Mongolia (Public Security Foundation 208096), and Oversea Returned Talent Start-up Funding for Research of Ministry of Education of China (208138), Inner Mongolia University Funds (10013-121008).

References

[1] International Agency for Research on Cancer, IARC Monographs on the Evaluation of the Carcinogenic Risk of Chemicals to Humans, Some Industrial Chemicals and Dyestuffs, Lyon, France, 29, 1982, p. 416.
[2] Agency for Toxic Substance and Disease Registry, Public Health Services, U.S. Department of Health and Human Services, Toxicological Profile for Formaldeyhde, NTIS Accesssion No. PB99-166654, 1991, p. 451.
[3] J. Zhang, Y. Jin, C. Li, Y. Shen, L. Han, Z. Hu, X. Di, Z. Liu, Appl. Catal. B: Environ. 91 (2009) 11.
[4] L.F. Liotta, Appl. Catal. B: Environ. 100 (2010) 403.
[5] C. Li, Y. Shen, M. Jia, S. Sheng, M.O. Adebajo, H. Zhu, Catal. Commun. 9 (2008) 355.
[6] Y. Shen, X. Yang, Y. Wang, Y. Zhang, H. Zhu, L. Gao, M. Jia, Appl. Catal. B: Environ. 79 (2008) 142.
[7] C. Ma, D. Wang, W. Xue, B. Dou, H. Wang, Z. Hao, Environ. Sci. Technol. 45 (2011) 3628.
[8] X. Tang, J. Chen, Y. Li, Y. Li, Y. Xu, W. Shen, Chem. Eng. J. 118 (2006) 119.
[9] X. Tang, J. Chen, X. Huang, Y. Xu, W. Shen, Appl. Catal. B: Environ. 81 (2008) 115.
[10] H. Huang, D.Y.C. Leung, ACS Catal. 1 (2011) 348.
[11] H. Huang, D.Y.C. Leung, J. Catal. 280 (2011) 60.
[12] L. Wang, M. Sakurai, H. Kameyama, J. Hazard. Mater. 167 (2009) 399.
[13] N. An, Q. Yu, G. Liu, S. Li, M. Jia, W. Zhang, J. Hazard. Mater. 186 (2011) 1392.
[14] Y. Zhang, Y. Shen, X. Yang, S. Sheng, T. Wang, M.F. Adebajo, H. Zhu, J. Mol. Catal. A: Chem. 316 (2010) 100.
[15] Y.-C. Hong, K.-Q. Sun, K-H. Han, G. Liu, B.-Q. Xu, Catal. Today 158 (2010) 415.
[16] V.A. de la Peña O'Shea, M.C. Álvarez-Galván, J.L.G. Fierro, P.L. Arias, Appl. Catal. B: Environ. 57 (2005) 191.
[17] A.J. Paine, Macromolecules 23 (1990) 3109.
[18] K.P. Lok, C.K. Ober, Can. J. Chem. 63 (1985) 206.
[19] A. Stein, Micropor. Mesopor. Mater. 44–45 (2001) 27.
[20] Q. Wu, Y. Shen, J. Liao, Y. Li, Mater. Lett. 58 (2004) 2688.
[21] S. Li, J. Zheng, W. Yang, Y. Zhao, Y. Liu, J. Porous Mater. 15 (2008) 589.
[22] Y. Zhang, Z. Lei, J. Li, S. Lu, New J. Chem. 25 (2001) 1118.
[23] S. Imamura, Y. Uematsu, K. Utani, T. Ito, Ind. Eng. Chem. Res. 30 (1991) 18.
[24] S. Imamura, Y. Uematsu, K. Utani, T. Ito, Catal. Lett. 24 (1994) 377.
[25] C. Zhang, H. He, Catal. Today 126 (2007) 345.
[26] X. Yang, Y. Shen, Z. Yuan, H. Zhu, J. Mol. Catal. A: Chem. 237 (2005) 224.
[27] G.Y. Popova, T.V. Andrushkevich, Y.A. Chesalov, E.S. Stoyanov, Kinet. Catal. 6 (2000) 885.
[28] C.F. Mao, M.A. Vannice, J. Catal. 154 (1995) 230.
[29] S. Scirè, S. Minicò, C. Crisafulli, C. Satriano, A. Pistone, Appl. Catal. B: Environ. 40 (2003) 43.
[30] H.C. Yao, Y.F.Y. Yao, J. Catal. 86 (1984) 254.
[31] A. Trovarelli, G. Dolcetti, C. de Leitenburg, J. Kaspar, P. Finetti, A. Santoni, J. Chem. Soc.: Faraday Trans. 88 (1992) 1311.
[32] S.A.C. Carabineiro, A.M.T. Silva, G. Dražić, P.B. Tavares, J.L. Figueiredo, Catal. Today 154 (2010) 21.
[33] Y. Xia, H. Dai, L. Zhang, J. Deng, H. He, C.T. Au, Appl. Catal. B: Environ. 100 (2010) 229.
[34] A.M. Venezia, G. Pantaleo, A. Longo, G.D. Carlo, M.P. Casaletto, F.L. Liotta, G. Deganello, J. Phys. Chem. B 109 (2005) 2821.
[35] J. Guzman, S. Carrettin, A. Corma, J. Am. Chem. Soc. 127 (2005) 3286.
[36] Q. Fu, S. Kudriavtseva, H. Saltsburg, M. Flytzani-Stephanopoulos, Chem. Eng. J. 93 (2003) 41.
[37] B. Campo, C. Petit, M.A. Volpe, J. Catal. 254 (2008) 71.

[38] S. Lai, Y. Qiu, S. Wang, J. Catal. 237 (2006) 303.
[39] C. Zhang, H. He, K.-I. Tanaka, Appl. Catal. B: Environ. 65 (2006) 37.
[40] M. Jia, H. Bai, Zhaorigetu, Y. Shen, Y. Li, J. Rare Earths 26 (2008) 528.
[41] J. Guo, Z. Hou, J. Gao, X. Zheng, Fuel 87 (2008) 1348.
[42] J. Gao, J. Guo, D. Liang, Z. Hou, J. Fei, X. Zheng, Int. J. Hydrogen Energy 33 (2008) 5493.
[43] C. Binet, M. Daturi, J.-C. Lavalley, Catal. Today 50 (1999) 207.
[44] E.D. Park, J.S. Lee, J. Catal. 186 (1999) 1.